Supplementary Information for the manuscript titled "Geoelectrical signatures of reactive mixing: a theoretical assessment"

Uddipta Ghosh[1,2], Tanguy Le Borgne[1], Damien Jougnot[3], Niklas Linde[4], and Yves Méheust[1]

[1] *Université de Rennes 1, CNRS, Géosciences Rennes UMR6118, 35042 Rennes, France*

[2] *Dept. of Mechanical Engineering, Indian Institute of Technology Gandhinagar, Palaj - 382355, Gujrat, India*

[3] *Sorbonne Universités, UPMC Univ. Paris 06, CNRS, EPHE, UMR 7619 METIS, Paris, France*

[4] *University of Lausanne, Applied and Environmental Geophysics Group, Institute of Earth Sciences, Lausanne, Switzerland*

In this supplementary material we provide more details about the physical description of the system, examples of geochemical reactions for which products are significantly more electrically conductive than reactants, the solution procedure of the transport equations, the derivation of short and long time scalings for the time evolution of the effective electrical conductivity (σ_{eff}), an illustration of the concentration and conductivity fields for stratified flows and finally discuss the consequences of the assumptions made in the present analysis and try to establish a link between the theory and possible laboratory experiments that can be performed to test the reliability of the current method.

S1 Physical description of the system

S1.1 Schematic representation

A schematic representation of the system is shown in Fig. 1 in the Letter. We refer to it in particular for the definition of the "electrode configurations", which we have labeled Parallel, Mixed, and Normal configurations. Note that these refer to idealised measurements configurations that are only possible in the laboratory. Nevertheless, they are very useful to gain conceptual insights.

S1.2 Chemical reactions that enhance the fluid's electrical conductivity

Several examples of reactions of the type $A + B \rightarrow C$ for which the electrical conductivities of the products C (which may be composed of several anions E^- and cations D^+) are much larger than those of the reactants are given in Table S1 together with the related conductivity data.

Some of these reactions involve a dehalogenation reaction of organic compounds (such as Trichloroethylene or TCE, Perchloroethylene or PCE, or Pentachlorophenol or PCP), as mentioned in A-type or C-type reactions in the table. These are used in remediation methods for the removal of contaminants [*Sundstrom et al.*, 1986; *Hort et al.*, 2014; *Venkatadri and Peters*, 1993], and are therefore of relevance to Geosciences. When the said organic matter is oxidized, it usually releases the halogen as anions and hence results in products with higher electrical conductivities. Most of these organic reactants have very low electrical conductivity. The oxidation can be carried out by oxidizing agents such as H_2O_2 or MnO_4^-, or other anions such as Lactate. Note that, since H_2O_2 itself is poorly conducting, reactions between halogenated organic compounds and Hydrogen Peroxide can result in large increases in the electrical conductivity through the production of H^+ and Cl^- ions. This is in contrast to the case when anions are used as the oxidizing agents, in which case the increase in the electrical conductivity is not as drastic, as evidenced by the modest values of $\sigma_r \sim O(10^{-1}) - O(10^{-2})$ in reactions A.3 and C in Table S1. However, oxidation with H_2O_2 also needs activation from iron

Table S1: Reactions producing ionic species and related conductivity data[a]

Reactions	**Conductivity data** (σ'_B, σ'_0 and σ_r)
A. *Oxidation of Halogenated Organic Compounds* [*Sundstrom et al.*, 1986; *Venkatadri and Peters*, 1993; *Gates and Siegrist*, 1995; *Hort et al.*, 2014; *Asgari et al.*, 2014]	Data taken from [*Haynes*, 2014]
(1)[b] C_2HCl_3 (TCE) + $H_2O_2 \longrightarrow CO_2 + H_2O + H^+ + Cl^-$	$\sigma'_B = \sigma'_{H_2O} \sim 10^{-4} - 10^{-6}$ S/m; $\sigma_0 = \sigma'_{H^+} + \sigma'_{Cl^-} = 42$ S/m $\sigma_r = \sigma'_B/\sigma'_0 \sim 10^{-4} - 10^{-7}$
(2)[b] C_2Cl_4 (PCE) + $H_2O_2 \longrightarrow CO_2 + H_2O + H^+ + Cl^-$	$\sigma'_B = \sigma_{H_2O} \sim 10^{-4} - 10^{-6}$ S/m; $\sigma_0 = \sigma'_{H^+} + \sigma'_{Cl^-} \sim 42$ S/m $\sigma_r = \sigma'_B/\sigma_0 \sim 10^{-4} - 10^{-7}$
(3)[c] $C_2HCl_3 + MnO_4^- \longrightarrow MnO_2 + CO_2 + H^+ + Cl^-$	$\sigma'_B = \sigma'_{MnO_4^-} \sim 6.1$ S/m; $\sigma_0 = \sigma'_{H^+} + \sigma'_{Cl^-} \sim 42$ S/m $\sigma_r = \sigma'_B/\sigma_0 \sim 10^{-1}$
(4)[b] C_6Cl_5OH (PCP) + $H_2O_2 \xrightarrow{Fe(s)} C_6H_5OH$ (Phenol) + Cl^- $C_6H_5OH + H_2O_2 \xrightarrow{Fe(s)} CH_3COO^- + H^+ + H_2O$	$\sigma'_B = \sigma'_{H_2O} \sim 10^{-4} - 10^{-6}$ S/m; $\sigma_0 = \sigma'_{H^+} + \sigma'_{Cl^-} + \sigma'_{CH_3COO^-} \sim 46$ S/m $\sigma_r = \sigma'_B/\sigma_0 \sim 10^{-4} - 10^{-7}$
B. *Corrosion of Iron* [*Zhang*, 2003]	Data from [*Haynes*, 2014]
(1)[b,d] $Fe^{(0)} + O_2 + H_2O \longrightarrow Fe^{2+} + OH^-$	$\sigma'_B = \sigma_{H_2O} \sim 10^{-4} - 10^{6}$ S/m $\sigma'_0 = \sigma'_{Fe^{2+}} + \sigma'_{OH^-} \sim 25$ S/m $\sigma_r \sim 10^{-4} - 10^{-6}$
(2)[b,d] $Fe^{(0)} + 2\,H_2O \longrightarrow Fe^{2+} + OH^- + H_2$	$\sigma'_B = \sigma_{H_2O} \sim 10^{-4} - 10^{6}$ S/m $\sigma'_0 = \sigma'_{Fe^{2+}} + \sigma'_{OH^-} \sim 25$ S/m $\sigma_r \sim 10^{-4} - 10^{-6}$
C. *Other dehalogenation reactions* [*Azizian and Semprini*, 2017]	Data from [*Haynes*, 2014]
(1)[c] $CCl_4 + C_3H_5O_3^-$ (Lactate) $\longrightarrow CHCl_3 + H^+ + Cl^- + CO_2 + HCO_3^-$	$\sigma'_B = \sigma_{C_3H_5O_3^-} \sim 3.8$ S/m; $\sigma'_0 = \sigma'_{H^+} + \sigma'_{Cl^-} + \sigma'_{HCO_3^-} \sim 47$ S/m $\sigma_r \sim 10^{-1} - 10^{-2}$
(2)[c] $CCl_4 + C_3H_5O_3^- \longrightarrow CHCl_3 + H^+ + Cl^- + CO_2 + HCO_3^-$	$\sigma'_B = \sigma_{C_3H_5O_3^-} \sim 3.8$ S/m; $\sigma'_0 = \sigma'_{H^+} + \sigma'_{Cl^-} + \sigma'_{HCO_3^-} \sim 47$ S/m $\sigma_r \sim 10^{-1} - 10^{-2}$
D. *Gas removal reactions - detoxification* [*Martin and Damschen*, 1981]	Data from [*Haynes*, 2014]
(1)[b,e] $Cl_2 + H_2O_2 \longrightarrow O_2 + H^+ + Cl^-$	$\sigma'_B = \sigma'_{H_2O} \sim 10^{-4} - 10^{-6}$ S/m; $\sigma'_0 = \sigma'_{H^+} + \sigma'_{Cl^-} \sim 42$ S/m $\sigma_r \sim 10^{-5}$
(2)[b,e] $SO_2 + H_2O_2 \longrightarrow H_2SO_4 \longrightarrow 2\,H^+ + SO_4^{2-}$	$\sigma'_B = \sigma'_{H_2O} \sim 10^{-4} - 10^{-6}$ S/m; $\sigma'_0 = \sigma'_{H_2SO_4} \sim 39$ S/m $\sigma_r \sim 10^{-5}$

[a] All conductivity data have been calculated for 1 Molar solutions at 25^0 C,
[b] Reactants are very poorly conducting, hence their conductivity is considered identical to that of water,
[c] One of the reacting species is conducting, so the electrical conductivity of the reactants has been taken as the conductivity of that species, for example that of MnO_4^- in reaction A.3,
[d] Very slow reactions, i.e., very low Damköhler number,
[e] One of the reactants can be dissolved gas in water (e.g., Cl_2 in D.1).

or other external sources such UV rays [*Venkatadri and Peters*, 1993]. Other possible reactions such as those in B-type or, D-type reactions require the presence of reactive solids or dissolved gases in water and can be rather slow reactions (e.g. the corrosion reactions in B).

We present in Table S2 the possible range of the Damköhler number (Da, see its definition in the main article) for some selected reactions given in Table S1. For the sake of brevity, we have specified the ranges of Da for only one of the reactions from each category (i.e., A, B, C and D) presented in Table S1. For all the reactions, the length scale has been taken as $w_0' \sim 1$ – 10 cm. The values of the diffusion coefficient lie around $D \sim 10^{-9}$ m^2/s for most species, see [*Haynes*, 2014]. The value of Da also depends on the reference concentration, c_0', which has been taken in the range $c_0' \sim 1$ µM – 1 M, since the various species have a wide range of solubility in water. From the values of Da given in Table S2, we note that Da can indeed have a very large range of values. For instance, while Da can be as low as $\sim 10^{-8}$ for Iron corrosion (very slow reactions), it can also be as high as $Da \sim 10^{12}$ for oxidation using peroxides, which are typically very strong oxidants (very fast reaction). We further note that the Péclect number (Pe) for these reactions mainly depends on the coefficients of diffusivity, the velocity (v_c) and the length scales (w_0'). For all the reactants, the diffusivity usually lies in the range $D \sim 10^{-9}$ m^2/s [*Haynes*, 2014]. Therefore, Pe can have a wide range of values depending on the choice of the velocity and length scales. For instance, with $v_c \sim 10^{-6}$m/s, as suggested by *Beven and Germann* [1982], one finds $Pe = v_c w_0'/D \sim 10 - 100$, for all the reactions in Table S2.

Finally, we note that the conductivity data have been given by assuming the reactions to be ideal, that is, we have assumed that no other ionic species and/or, electrically conducting elements, are present that can influence the local electrical conductivity in any significant way. It is also important to note that in field scale measurements many of these reactions might bring about other unintended effects, which is not possible to account for in the current analysis. For instance, in the oxidation reaction of TCE using Permanganate (see reaction A.4 in Table S1), the Hydrogen

Table S2: Dimensionless number-space for some selected reactions from Table S1[a].

Reactions	**Physical Properties & non-dimensional number space**
A. *Oxidation of Halogenated Organic Compounds*	Data taken from [*Rossi et al.*, 2015; *Sundstrom et al.*, 1986]
(1)[b] C_2HCl_3 (TCE) + $H_2O_2 \longrightarrow CO_2 + H_2O + H^+ + Cl^-$	$D_{\mathrm{TCE}} \sim 10^{-9}$ m^2/s $K \sim 10^{-3} - 10^{-2}$ (mol.s/lt)$^{-1}$ $Da = Kc_0'w_0^2/D_{\mathrm{TCE}} \sim 10^{-6} - 10^4$
B. *Corrosion of Iron*	Data taken from [*Patil and Sharma*, 2011; *Haynes*, 2014]
(1)[b,c] $Fe^{(0)} + O_2 + H_2O \longrightarrow Fe^{2+} + OH^-$	$D_{\mathrm{O_2}} \sim 2.4 \times 10^{-9}$ m^2/s $K \sim 10^{-6}$ (mol.s/lt)$^{-1}$ $Da = Kc_0'w_0^2/D_{\mathrm{O_2}} \sim 10^{-8} - O(1)$
C. *Other dehalogenation reactions*	Data taken from [*Nakanishi*, 1978; *Azizian and Semprini*, 2017]
(1)[b] $CCl_4 + C_3H_5O_3^-$ (Lactate) $\longrightarrow CHCl_3 + H^+ + Cl^- + CO_2 + HCO_3^-$	$D_{\mathrm{CT}} \sim 10^{-9}$ m^2/s $K \sim 1.2 \times 10^{-5}$(mol.s/lt)$^{-1}$ $Da = Kc_0'w_0^2/D_{\mathrm{TCE}} \sim 10^{-6} - 10^2$
D. *Gas removal reactions - detoxification*	Data taken from [*Martin and Damschen*, 1981; *Haynes*, 2014]
(1)[b,d] $SO_2 + H_2O_2 \longrightarrow H_2SO_4 \longrightarrow 2\,H^+ + {SO_4}^{2-}$	$D_{\mathrm{SO_2}} \sim 1.6 \times 10^{-9}$ m^2/s $K \sim 8 \times 10^5$ (mol.s/lt)$^{-1}$ $Da = Kc_0'w_0^2/D_{\mathrm{SO_2}} \sim 8 \times 10^4 - 8 \times 10^{12}$

[a] In all the cases the typical length scale is chosen as $w_0 \sim 1 - 10$ cm. The reference concentration has been taken in the range: $c_0' \sim 1$ M $- 1$ μM, since the solubility of various species vary widely. All the data have been calculated at 25^0 C.

[b] The reference diffusivity has been taken as that of the limiting species, namely for TCE in A, O_2 in B, CCl_4 in C and SO_2 in D.

[c] An extremely slow reaction.

[d] Extremely fast reaction.

ions are often adsorbed in the subsurface porous media [*Hort et al.*, 2014], which can decrease the electrical conductivity significantly [*Hort et al.*, 2014]. Therefore, in essence, the efficacy of the foresaid reactions is best evaluated by dedicated laboratory experiments.

S1.3 Bulk conductivity vs. the role of EDLs

The production of ions by reactions in the porous media can influence the local conductivities in mainly two ways. First, the presence of highly mobile ions changes the local conductivity, also termed the pore space electrical conductivity. This is a relatively simple and near-linear effect [*Squires and Bazant*, 2004] for dilute solutions. Second, surface conductivity effects come into play when the surface active agents present on the grain surfaces (e.g. silica [*Waxman et al.*, 1968; *Revil and Leroy*, 2004]) absorb either negative or positive ions to impart the grains their own surface charge [*Wang and Revil*, 2010]. These effects become particularly prominent in presence of clay materials. As a result of this, counterions concentrate around the grains in high numbers and create an Electrical Double Layer (EDL) [*Revil and Glover*, 1997; *Ghosh et al.*, 2017]. EDLs naturally enhance the conductivity of a porous media, since they contain high concentrations of net charge. In short, the enhancement in conductivity arises from two sources in the most general case, namely, (1) an enhancement of the local conductivity due to addition of ions to the pore solution and (2) the creation of highly charged EDLs around solid grains, which enhances the local conductivity of the pore solution in their vicinity.

In case that EDLs are present in a porous medium (as is the case at most interfaces between mineral surfaces and aqueous liquids), one may apply the Differential Effective Medium Approach (DEMA) (e.g. [*Leroy et al.*, 2017]) to evaluate the local equivalent conductivity of the pore space, which aptly accounts for both bulk conductivity and the excess conductivity from the EDLs. In the DEMA, the excess conductance in the EDL is modelled as a surface conductivity of the solid grains in the porous media. In this study, we choose to neglect the formation of EDL and assume that the ions produced by the reaction only modify the local water conductivity through the first mechanism,

that is, only by changing the local conductivity of the bulk fluid. The local conductivity in the pore space is then expressed as [*Revil*, 1999]: $\sigma'_{\mathrm{f}} = \sigma'_{\mathrm{b}} + 2\nu' e^2 c'_C$, where c'_C is the local concentration of the product, ν' is the mobility of the ions, e is the protonic charge and σ'_{b} is the background conductivity of pore fluid. When accounting for the porosity and the connectivity of the pore space, the effective local conductivity can be expressed as [*Archie et al.*, 1942]: $\sigma' = \sigma'_{\mathrm{f}}/F$, where F is the formation factor [*Revil and Glover*, 1997], given by: $F = \varphi^{-m}$, where φ is the porosity and m is the cementation exponent. A detailed analysis of effective conductivity change resulting from the effects of EDLs is the subject of future work.

S1.4 Flow heterogeneity

We assume that the front is subjected to a stratified flow with a velocity field given by $\mathbf{v}' = u'(y')\,\mathbf{e}_x$, where $u(y)$ can be an arbitrary function of y, the coordinate parallel to the initial planar interface between the two reactive solutions. A particular case of such flow is simple shear flow, in which $u'(y') \propto y'$. In this regard it is important to note that any unidirectional velocity profile near a location $\mathbf{x}'_0$ can be expressed as [*Leal*, 2007], $\mathbf{v}' = \mathbf{v}'_0 + \mathbf{E}'\cdot(\mathbf{x}' - \mathbf{x}'_0) + \mathbf{K}' : (\mathbf{x}' - \mathbf{x}'_0)(\mathbf{x}' - \mathbf{x}'_0) + ...$, which can be recast as, $\mathbf{v}' = \mathbf{v}'_0 + \mathbf{G}'(\mathbf{x}')\cdot(\mathbf{x}' - \mathbf{x}'_0)$. Note that here, $\mathbf{v}'_0 = \mathbf{v}'(\mathbf{x}'_0)$ and $\mathbf{G}' = \mathbf{E}' + \mathbf{K}'\cdot(\mathbf{x}' - \mathbf{x}'_0) + ...$. For locations sufficiently close to $\mathbf{x}'_0$, we find, $\mathbf{G}' \sim \mathbf{E}'(\mathbf{x}'_0)$. Here $\mathbf{E}' = \boldsymbol{\nabla}\mathbf{v}'$ is the velocity gradient tensor. Considering a unidirectional flow, where $\mathbf{v}' = u'(y')\mathbf{e}_x$, it can be easily deduced that $E_{\mathrm{xy}} = (du'/dy')_{y'=y'_0}$, while all other components of $\mathbf{E}'$ vanish. Therefore, for a unidirectional flow, the above expression for velocity simply becomes, $u' = u'(y'_0) + (du'/dy')_{y'=y'_0}(y' - y'_0)$, while all other velocity components are naturally zero. Here, without loss of generality, we can establish our origin at $y' = y'_0 = 0$ and assume $u'(y'_0) = 0$ (this is equivalent to taking an inertial frame moving with velocity $u'(y'_0)$). As such, the expression for the velocity around $y'_0 = 0$ can be further simplified as, $u'(y') = \Gamma' y'$, with $\Gamma' = (du'/dy')_{y'=y'_0}$. This constitutes the fundamental description of shear flow as used in the main manuscript. Therefore, to summarize, in the present work we consider that the

essential physics of how reactive mixing impacts the effective conductivity is best captured by first investigating the said problem for a simple shear flow $\Gamma' = \Gamma_0 = \left(\frac{du'}{dy'}\right)_{y'=0}$, as previously considered by Bandopadhyay et al.[*Bandopadhyay et al.*, 2017] to characterize reactive mixing dynamics.

S2 Mathematical description of the system

S2.1 Dimensional equations

We detail here the dimensional governing equations that are given in non-dimensional form in the main manuscript. In the following we use "dashed" symbols to denote dimensional variables. The transport equations for the reactants and the products are:

$$\frac{\partial c_i'}{\partial t'} + \mathbf{v}' \cdot \nabla c'_i = D_i \nabla^2 c_i' + R_i' \ , \tag{S1}$$

where D_i is the molecular diffusion coefficient of the i-th species and the source/sink terms, while R_i' denote the respective reaction rates. For the reactants these are given by, $R_A' = R_B' = -K c_A' c_B'$, for the products by: $R_C' = K c_A' c_B'$. The above species transport equations are subject to the following initial and boundary conditions, which remain valid in all three configurations:

(a) Initial conditions:

$$\text{At } t' = 0,\ c_A' = c_0' \ \forall\ x' < 0 \text{ and } c_A' = 0 \ \forall\ x' > 0 \tag{S2a}$$

$$c_B' = 0 \ \forall\ x' < 0 \text{ and } c_B' = c_0' \ \forall\ x' > 0 \tag{S2b}$$

$$c_C' = 0 \ \forall\ x' \tag{S2c}$$

(b) Boundary conditions:

$$c'_A = c'_0,\ c'_B = 0,\ \text{at } x' \to -\infty \tag{S3a}$$

$$c'_A = 0,\ c'_B = c'_0,\ \text{at } x' \to \infty \tag{S3b}$$

$$c'_C = 0 \text{ at } x' \to \infty \text{ and } -\infty \tag{S3c}$$

We can now evaluate the effective conductivity. Following a number of previous studies [*Maineult et al.*, 2017], we express that the potential difference applied across the domain (as shown in the three configurations) drive a current through the pores, of increasing magnitude in time as the reaction progresses. The potential distribution in the domain would thus emerge from the requirement of current conservation. The current density $\mathbf{i}'$ at a given location is related to the local conductivity σ' and local electrical potential ϕ' through: $\mathbf{i}' = -\sigma'\nabla\phi'$, with $\sigma' = F^{-1}\left(\sigma_{\mathrm{b}} + 2\nu' e^2 c'_D\right)$. Therefore, the requirement of current conservation translates into the following equation for the electrical potential:

$$\nabla \cdot (\sigma'\nabla\phi') = 0\ . \tag{S4}$$

The potential is subject to the following boundary conditions:

$$\text{Parrallel Configuration: } \phi'(0, y') = 0;\ \ \phi'(L'_x, 0) = -\Delta V; \quad \text{At } y' = \pm L'_y,\ \frac{\partial \phi'}{\partial y'} = 0; \tag{S5a}$$

$$\text{Mixed Configuration: } \phi'(x', L'_y) = -\Delta V;\ \phi'(x', -L'_y) = 0; \quad \text{At } x' = \pm L'_x,\ \frac{\partial \phi'}{\partial x'} = 0; \tag{S5b}$$

$$\text{Normal Configuration: At } z' = -L'_z,\ \phi' = -\Delta V; \qquad \text{At } z' = L'_z,\ \phi' = 0; \tag{S5c}$$

where we have assumed that a potential difference of ΔV is applied across the domain. Note that in the normal configuration the potential difference is applied along the z-axis, so the boundary conditions along the x and y-axes become inconsequential.

Finally, the effective conductivities of the entire domain are defined as

$$\sigma'_{\text{eff},k} = \frac{\Delta V A'_{\text{el},k}}{L'_k I'_{\text{el},k}};\ \text{where } I'_{\text{el},k} = \int_{\text{electrode}} \sigma' \nabla \phi' \cdot \mathbf{n}_k dS' \tag{S6}$$

where $k = 1$ denotes the Parallel Configuration, $k = 2$ the Mixed Configuration, and $k = 3$ the Normal Configuration, $A'_{\text{el},k}$ is the area of the electrode receiving the current. For configuration denoted by index k, $I'_{\text{el},k}$ is the total current through the cross-section of the electrode, and $\mathbf{n}_k$ is the normal vector to the electrode surface. The above expression evaluates the total current at the electrode with the lower potential (i.e., the one which receives the current) and computes the effective conductivity as the ratio of the applied potential difference to this current. Note that the ionic species should also be subject to electromigration forces in the presence of externally applied field. We have neglected these forces in (S1). This is because, firstly, the bulk is assumed to be electroneutral and second, one can apply the well-known weak field approximation to ignore the electromigration terms as a first approximation.

One can now make the equations above dimensionless with respect to proper characteristic scales for all relevant variables. This procedure is explained in the Letter, where the dimensionless governing equations, describing the evolution of species concentrations as well as that of the electrical potential and current, are given. The Péclet and Damköhler number naturally arise as prefactor to different terms in these dimensionless transport equations.

S2.2 Solution procedure for the transport equations

S2.2.1 Solution of the transport equation using a coordinate transformation

The lamellar mixing theory is a Lagrangian method that allows quantifying the effect of the mixing front deformation by velocity gradients on the enhancement of diffusive mixing [*Le Borgne et al.*, 2014, 2015]. We first move to a new coordinate system (n, ρ) attached to the reactive front, as

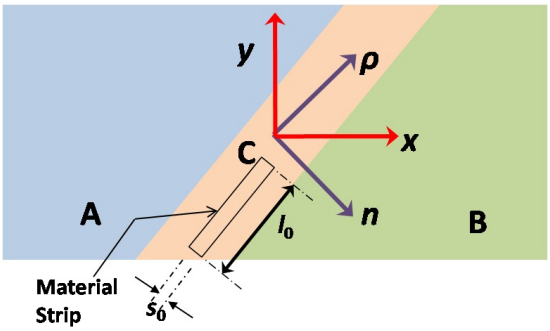

Figure S1: Schematic representation of the lamellar coordinate attached to the reaction front. We denote the coordinate attached to the domain as the Cartesian (x, y) system. The lamella coordinate system is (n, ρ), where n is normal to the reaction front and ρ is parallel to the front.

depicted in Fig. S1. The origin of this new coordinate system always coincides with the center of the lamella/strip; the n-axis is perpendicular to the strip at all time, while the ρ-axis is parallel to the strip. Since the front width is much smaller than its length, the variations along the n-axis are much stronger than those along the ρ-axis, so that the ρ-gradients may be neglected as compared to the n-gradients: $\frac{\partial}{\partial n} \gg \frac{\partial}{\partial \rho}$ and $\frac{\partial^2}{\partial n^2} \gg \frac{\partial^2}{\partial \rho^2}$. The velocity can be expressed in the new coordinate system as follows: $\mathbf{v} = v_n \mathbf{e}_n + v_\rho \mathbf{e}_\rho$, where v_i is the velocity component along the i-th axis and $\mathbf{e}_i$ is the corresponding unit vector. In this new coordinate system the species transport equation for A is now expressed as

$$\frac{\partial c_A}{\partial t} + v_n \frac{\partial c_A}{\partial n} = \frac{\partial^2 c_A}{\partial n^2} - Da\,(c_A c_B) \tag{S7}$$

If one considers a convective strip within the reaction front of initial width s_0 and length at time t, $l(t)$, with $l(0) = l_0$ (Figure S1), the total volume of the strip is (unit depth) $V_s = l_0 s_0$. The strip is oriented along the front and hence it is lengthwise parallel to the ρ-axis. Then its rate of stretching is given by [*Bandopadhyay et al.*, 2017]:

$$\frac{1}{l}\frac{dl}{dt} = \frac{Pe^2\Gamma^2(y)\,t}{1 + Pe^2\Gamma^2(y)\,t^2} \;\Rightarrow\; l(t) = l_0\sqrt{1 + Pe^2\Gamma^2(y)\,t^2} \tag{S8}$$

Since $l\,s = l_0\,s_0$, this means that the width of the strip at a given time is given by:

$$s\,(t) = \frac{s_0}{\sqrt{1 + Pe^2\Gamma^2\,(y)\,t^2}} \tag{S9}$$

The entire reaction front can now be decomposed into a combination of several such strips, with different degrees of stretching. The location of the strips at a given time can be computed by tracking the locations of the strip-centres with a particle tracking scheme, as previously shown by *Meunier and Villermaux* [2010]. For instance, the location of the k-th component of the strip, $\mathbf{x}_k\,(t)$, is given by the equation:

$$\frac{d\mathbf{x}_k}{dt} = Pe\,\mathbf{v}\,(\mathbf{x}_k) \tag{S10}$$

The stretching rate for the k-th stripe is determined by the local rate of shear, $\Gamma\,(y_k)$. The n-component of the velocity is given by: $v_n = -\frac{n}{s}\frac{ds}{dt}$ [*Le Borgne et al.*, 2014; *Meunier and Villermaux*, 2010]. Defining the so-called *warped time* τ and a normalized coordinate z as follows [*Le Borgne et al.*, 2014]:

$$\tau = \int_0^t \frac{du}{s\,(u)^2} \quad \text{and} \quad z = \frac{n}{s}\,, \tag{S11}$$

and applying a change of coordinates from (n, t) to (z, τ) in (S7), we obtain the transport equation in the form [*Le Borgne et al.*, 2014]:

$$\frac{\partial c_A}{\partial \tau} = \frac{\partial^2 c_A}{\partial z^2} - s^2\,(t)\,Dac_A c_B \quad . \tag{S12}$$

The transport equations for the other species have analogous forms. For an arbitrary flow one can apply the Diffusive Strip Method [*Meunier and Villermaux*, 2010], wherein the number of individual strips has to be increased as the background flow stretches the reaction front more and more with time.

The next step in evaluating the concentrations is to reconstruct the said field in the (x, y) coor-

dinate system. We discuss the reconstruction for a shear flow in the next subsection.

S2.2.2 Particular case of a linear Shear Flow

We now consider the particular case of a simple shear flow where $\Gamma(y) = 1$ across the domain. In the paper the results are presented for this kind of flow, since shear is a dominant deformation mechanism governing the dynamics of mixing fronts in heterogeneous porous media [*Le Borgne et al.*, 2014; *Bandopadhyay et al.*, 2017]. In particular, as mentioned in section S1.4, any stratified flow can be decomposed into a set of coexisting shear flows. For a simple shear flow, the (n, ρ) coordinate system becomes a rotating Cartesian-like system, where the unit vectors $\mathbf{e}_\rho$ and $\mathbf{e}_n$ have the same directions for the entire front. The entire front can then be treated as a single strip and hence the ρ coordinate becomes inconsequential, which enables us to write:

$$c_D(\mathbf{x}, t) = c_D(n, \tau) \tag{S13}$$

At time t, the coordinates n and $x - y$ are related in the following way:

$$n = x\left(\frac{1}{\sqrt{1 + Pe^2\, t^2}}\right) - y\left(\frac{Pe\, t}{\sqrt{1 + Pe^2\, t^2}}\right) \tag{S14}$$

For a simple shear flow, the strip width and the wrapped time vary as follows [*Bandopadhyay et al.*, 2017]

$$s(t) = \frac{s_0}{\sqrt{1 + Pe^2 t^2}}; \text{ and } \tau = \frac{1}{s_0^2}\left(t + \frac{1}{3}Pe^2 t^3\right) \tag{S15}$$

With the above considerations we can solve for the species concentration from equation (S12) and its analogues. These reaction-diffusion equations have been solved numerically using a finite difference scheme, with a large spatial domain along x to ensure that boundary effects do not become significant. The resulting electrical potential can be used to evaluate the current and hence the effective conductivity based on Eq. (7) in the manuscript (i.e., the non-dimensional version of

eqn. (S6) herein). This procedure is used for the Parallel and Mixed configurations, the equation for potential being solved using a finite difference scheme in the $x-y$ domain. For the Normal configuration, the effective conductivity can be evaluated semi-analytically as discussed in the next subsection.

For further discussions on the reconstruction of the concentration distribution in cases of complex flows, one may look into the work of Meunier and Villermaux [*Meunier and Villermaux*, 2010].

S2.3 Effective conductivity for The Normal Configuration

In the Normal Configuration, the geometry combined with the relevant boundary conditions for the electrical potential (see eqn. (S5)c) enables us to write the effective conductivity of the whole domain in a semi-analytical form. This can be done by dividing the whole domain into parallel small strips of length $2L_z$ along the z-axis with area $dA = dx \times dy$. As such the resistance of such a small strip, located at (x, y) is given by: $R = 2L_z/\sigma dA$. Since all these elementary volumes are in parallel, the total effective conductivity is given by:

$$\sigma_{\text{eff},3} = \frac{\iint_S \sigma\,(x,y)\,dx\,dy}{\iint_S dx\,dy} = \sigma_{\text{avg}} \quad , \tag{S16}$$

where the integral spans the area of the medium in the $x-y$ plane. Note that $\sigma_{\text{eff},3}$, as per (S16), is also equal to the average conductivity of the domain. Further, noting that $\sigma = F^{-1}\,(\sigma_{\text{r}} + 2c_D)$, we can also infer that σ_{eff} is also linearly proportional to the mass of product that has appeared in the medium as a result of the reaction. This indicates that this configuration can be an efficient way to monitor the mass of product and hence the rate of the reaction in the subsurface.

S3 Scaling Analysis for the time evolution of the effective conductivity

In this section, we derive approximate scalings for the electrical conductivity in the three different configurations.

S3.1 The Parallel Configuration

We first consider the purely diffusive case for $Pe = 0$. In the parallel configuration (see Fig. 1 in the Letter), the zones of higher conductivity (i.e., the reaction front in the middle) and lower conductivity lie in series. Hence the effective conductivity has approximately the following form:

$$\sigma_{\text{eff}} = \frac{L_x}{L_y} \int_{-L_y}^{L_y} \left(\int_{-L_x}^{L_x} \sigma^{-1} dx \right)^{-1} dy \tag{S17}$$

In this purely diffusive situation, $\sigma = \sigma(x)$ and hence we obtain, $\sigma_{\text{eff}} = 2L_x \left(\int_{-L_x}^{L_x} \sigma^{-1} dx \right)^{-1}$. Let us denote the width of the highly conducting zone (i.e., the zone occupied by the product) as $2w(t)$. A large times, i.e., for $t \gg Da^{-1}$, the conductivity varies across the domain as $\sigma \sim \sigma_{\text{r}}$ for $x \geq w(t)$ and $x \leq -w(t)$ and $\sigma \sim 2c_D$ for $-w(t) \leq x \leq w(t)$. Here, we assume that at larger times in the region $-w(t) \leq x \leq w(t)$, the conductivity of the product dominates over the background conductivity, i.e. $c_D \gg \sigma_r$. Enforcing the said variation in conductivity, using the Mean Value Theorem, and assuming that $\sigma_{\text{r}} \ll \bar{c}_D$ and $w(t) \ll L_x$, we can deduce:

$$\int_{-L_x}^{L_x} \sigma^{-1} dx \sim \tfrac{2(L_x - w)}{\sigma_{\text{r}}} \left[1 + \tfrac{w\sigma_{\text{r}}}{2(L_x - w)\bar{c}_D} \right], \tag{S18a}$$

$$\implies \left(\int_{-L_x}^{L_x} \sigma^{-1} dx \right)^{-1} \sim \tfrac{\sigma_{\text{r}}}{2(L_x - w)} \left[1 - \tfrac{w\sigma_{\text{r}}}{2(L_x - w)\bar{c}_D} + ... \right] \sim \tfrac{\sigma_{\text{r}}}{2L_x} \left(1 - \tfrac{w}{L_x} \right)^{-1} + \text{O}(\sigma_r^2) \tag{S18b}$$

$$\implies \left(\int_{-L_x}^{L_x} \sigma^{-1} dx \right)^{-1} \sim \tfrac{\sigma_{\text{r}}}{2L_x} + \tfrac{\sigma_{\text{r}} w(t)}{2L_x^2} + \text{O}\left(w^2, \tfrac{\sigma_r^2}{\bar{c}_D} \right) \tag{S18c}$$

where $\bar{c}_D$ is the mean concentration of the product. From this we obtain

$$\sigma_{\text{eff}} = 2L_x \left(\int_{-L_x}^{L_x} \sigma^{-1} dx \right)^{-1} \sim \sigma_{\text{r}} + \frac{\sigma_{\text{r}} w(t)}{L_x} + \text{O}\left(w^2, \frac{\sigma_{\text{r}}^2}{\bar{c}_D} \right) \tag{S19a}$$

$$\implies \Delta\sigma_{\text{eff}} = \sigma_{\text{eff}} - \sigma_{\text{r}} \sim \frac{\sigma_{\text{r}} w(t)}{L_x} \tag{S19b}$$

The width $w(t)$ grows by diffusion as $w(t) \sim \sqrt{t}$ and hence $\Delta\sigma_{\text{eff}} \sim (\sigma_{\text{r}}/L_x)\sqrt{t}$. One remarkable feature of the above result is that the width of the product is the dominant term in the effective conductivity, while the concentration of the ions only contributes to the higher order terms.

In the presence of a velocity gradient ($Pe > 0$), equation (S19b) remains valid as long as the zones of high and low conductivity are approximately in series. When the reactive zone is strongly tilted this is not strictly true as a component of the current may flow parallel to the reactive zone. However, as verified in figure 3(a) of the letter, the scaling of equation (S19b) remains a good approximation for a broad range of Péclet numbers. For $Pe > 0$, diffusive broadening occurs along the n direction and projection in the x direction implies that $w(t) \sim \sqrt{1 + Pe^2\,\Gamma^2\,t^2}\sqrt{(}t) \sim Pe\,\Gamma\,t^{3/2}$. This leads to $\Delta\sigma_{\text{eff}} \sim t^{3/2}$, which is consistent with the scaling observed in figure 3(a) of the Letter. The above scaling predictions for the width $w(t)$ of the product distribution has also been verified in figure S2, where $w(t)$ has been plotted as a function of t for different values of Pe. Note that the $w \sim t^{1/2}$ for pure diffusion and $w \sim t^{3/2}$ for $Pe > 0$ is clearly indicated in this figure. It should be further noted that for $Pe > 0$, width of the highly conducting zone starts increasing at a faster rate as compared to pure diffusion after the shear time, $t \sim t_s = Pe^{-1}$. This is simply because for $t > t_s$, the term Pe^2t^2 in the factor $\sqrt{1 + Pe^2\,\Gamma^2\,t^2}$ becomes dominant.

S3.2 Mixed and Normal Configuration

Considering again first the case $Pe = 0$, the zones of high and low conductivity are in parallel in both the Mixed and Normal configurations. Focusing on such situations, we note that the effective

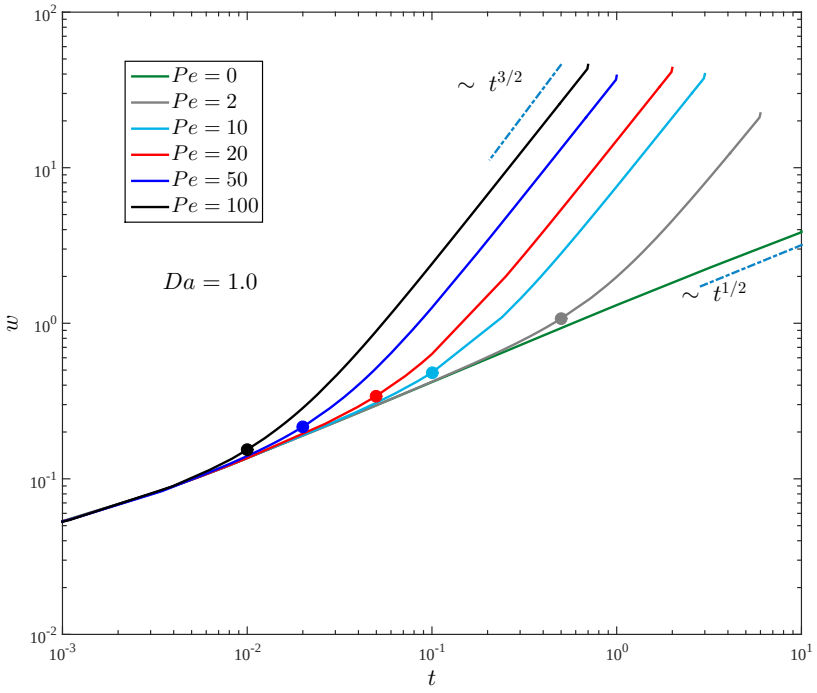

Figure S2: The width (w) of the highly conducting zone in the $x-y$ plane has been plotted as a function of time (t) for different values of Péclet number (Pe) as indicated in the legends, for $Da = 1.0$. The scaling prediction of $w \sim \sqrt{(t)}$ for $Pe = 0, t \gg Da^{-1}$ (diffusion) and $w \sim t^{3/2}$ for $Pe > 0, t \gg Pe^{-1}$ is verified in this figure. The circles denote the width at the shear time, $t_s = Pe^{-1}$. Note that the width of the conducting zones "takes-off" after $t \sim t_s$, when the effect of shear becomes prominent.

conductivity is given by:

$$\sigma_{\text{eff}} = \frac{1}{2L_x} \int_{-L_x}^{L_x} \sigma dx \tag{S20}$$

Enforcing the same distribution of the conductivity as in §S3.1 along with the stated assumptions, we can easily deduce, at large times ($t \gg Da^{-1}$), $\int_{-L_x}^{L_x} \sigma dx \sim 2\sigma_{\text{r}} (L_x - w) + 2\tilde{m}_c$, where $\tilde{m}_c = \int_{-L_x}^{L_x} c_D dx$ is the mass of the product per unit width of the domain. Hence it can be shown that:

$$\Delta\sigma_{\text{eff}} \sim \frac{\tilde{m}_c}{L_x} + \text{O}\left(\sigma_{\text{r}} w(t)\right) \tag{S21}$$

We thus conclude that in the Normal and Mixed Configurations and for $Pe = 0$, the effective conductivity is proportional to the mass of product. For pure diffusion the mass of product is expected to scale as $t^{1/2}$ [*Bandopadhyay et al.*, 2017]. We thus conclude that in this case $\Delta\sigma_{\text{eff}} \sim t^{1/2}$, for the normal and the mixed configurations, which is confirmed in figures 3b and 3c in the Letter.

In presence of velocity gradients, the proportionality between the effective conductivity and the mass of product is maintained at all times in the normal configuration (see Eq. (S16)), while in the mixed configuration, we expect the above scaling to hold at short times ($t < Pe^{-1}$), when the imposed flow has not tilted the reaction front by a significant amount. The mass of product in a mixing front submitted to a simple shear deformation has been studied by *Bandopadhyay et al.* [2017]. For $t < Pe^{-1}$, the effect of shear is negligible and the scaling derived for $Pe = 0$ are expected to hold. For $t > Pe^{-1}$, mixing is enhanced by shear and the mass of the product was shown to vary as, $\tilde{m}_c \sim \frac{Da}{4} t^{3/2}$ for $Pe < Da$, and $\tilde{m}_c \sim (DaPe/10\sqrt{3})\, t^{5/2}$ for $Pe > Da$. These scaling laws are verified for the effective conductivity in the normal configuration, as shown in figures 3(c) and 3(f) in the Letter. Note that, strictly speaking, these scaling laws should only hold for the normal configuration, for which the parallel arrangement of the high and low conductivity zones are always maintained. In the mixed configuration, the parallel arrangement is quickly violated owing to the flow driven tilting of the reaction front. Nevertheless, the scaling laws reported herein to the mixed configuration still approximately hold as depicted in figures 3(b) and 3(e) in the Letter. However, significant departure is observed during the intermediate times in the mixed configuration, which we have discussed in the letter. As a final note, we observe that $\Delta\sigma_{\text{eff}}$ is indeed sensitive to Da, that is, to the reaction kinetics (through the mass of the product) as evidenced from the above scaling analysis and observed in figures 3(e - f) of the Letter.

S3.3 Generalized Stratified Flow - Illustrative example

Fig. S3 compares the spatial distribution of the electrical current to that of conductivities for an illustrative example with sinusodially stratified flow of velocity field $u(y) = \sin(6\pi y/5L_y)$, in the Mixed Configuration. The values of the various system parameters are given in the figure caption. The current lines are curved near the reaction front, while they are nearly straight near the outer edges of the domain. This is because near the reaction front, the current tends to flow through

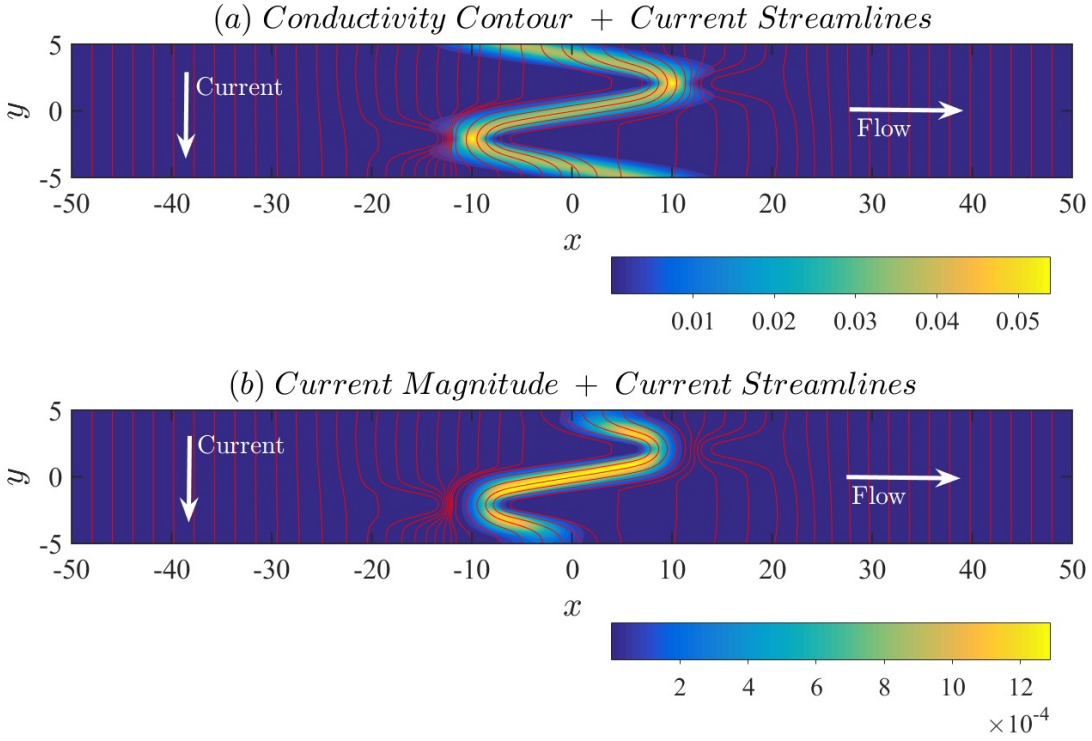

Figure S3: (a) Streamlines of the current and contour map of the electrical conductivity, for a sinusodially stratified flow defined as $u = \sin(6\pi y/5L_y)$, are shown at times $t = 1$, with $Pe = 20$ and $Da = 2$ in the mixed configuration, with $\sigma_r = 10^{-5}$, $L_x = 50$ and $L_y = 5$. (b) Magnitude of the current density, along with current streamlines, for the same scenario as in (a). In both (a) and (b), blue regions indicate lower magnitudes and yellow regions larger magnitudes of the variables in question.

the path of least resistance and hence tries to stick to the reaction front where the conductivity is higher. This assertion is verified in figure S3(b), where it can be observed that the current density magnitude is indeed the largest within the reaction front and has almost the exact shape as that of the front itself. Finally, we note that in Fig. S3(a) the zone of high conductivity (the yellow zone in the middle) almost identically represents the reaction front at any time.

S4 Further Discussions: Bridging the gap between theory and experiments

Our theoretical results provide new insights on the geoelectrical signatures of tracers designed to be highly sensitive to mixing processes. These results may be ultimately transferred to applications through the presented dimensionless numbers: the Damköhler number (Da), the Péclet number (Pe)

and the conductivity ratio (σ_r). Nevertheless, this theoretical method needs to be further developed before its predictions can be used to interpret laboratory or field scale experiments. A laboratory test of the present concept could be carried out either on a column-based setup, as previously done by *Day-Lewis et al.* [2017] and *Briggs et al.* [2014], or on a 2-D porous medium inside a flat Hele-Shaw-type geometry, as previously done by *Jougnot et al.* [2018]. Such an experiment would typically involve the design of a specific array of electrodes [*Day-Lewis et al.*, 2017]. Sheet-like or mesh electrodes can be used to ensure that the current injection is uniform (as assumed in the theory). The different configurations of electrical measurement may be constructed by inserting electrodes either at the ends (parallel) or towards the side of the experimental set up (mixed and normal config.). The measurements for σ_{eff} may be carried out by injecting current through the proper electrodes, and measuring the potential at the others, as required. Such laboratory scale experiments will be needed to validate the feasibility of the concept proposed herein and to make the proposed monitoring technique sufficiently reliable and robust for future field applications.

Shifting our focus to the assumptions undertaken herein, we note the following key points. (1) The background conductivity σ_r can have a wide range of magnitude depending on the presence of other ionic species in the pore water. One would thus need to consider solubility of the various reactants and solutes in water, as well as the number of ions they produce. (2) Here the electrodes have been assumed to be ideal and sheet-like, therefore spanning at least one side of the whole domain. This is again an idealization and in practice point electrodes are likely to be used, as done for ERT measurements [*Dahlin and Zhou*, 2004]. In this case, the boundary conditions for the potential, i.e., conditions 6(a) - 6(c) in the main manuscript would have a different form. (3) Another important point to note is that we have considered here a shear front, which might only represent a particular portion of a much larger mixing front, of complex geometry. For such a geometrically-complex mixing front, σ_{eff} would be controlled by the processes occurring over the entire mixing front, rather than over one particular region of the front. In such a configuration, the work presented herein would

rather serve to define anisotropic effective conductivities for the cells used in geoelectrical forward modeling and inversion. In other words, it would provide an upscaling procedure to obtain effective block values for different regions (of smaller scale) of the mixing front, which could then be used to solve a larger-scale ERT problem. (4) In addition, the environmental impact of the proposed reactions (see Table S1), as well as the quantity of reactants required to obtain detectable signals, have to be investigated further.

References

Archie, G. E., et al., The electrical resistivity log as an aid in determining some reservoir characteristics, *Transactions of the AIME*, *146*(01), 54–62, 1942.

Asgari, G., A. Seidmohammadi, and A. Chavoshani, Pentachlorophenol removal from aqueous solutions by microwave/persulfate and microwave/h 2 o 2: a comparative kinetic study, *J. Environ. Health Sci. Eng.*, *12*(1), 94, 2014.

Azizian, M. F., and L. Semprini, Simultaneous anaerobic transformation of carbon tetrachloride to carbon dioxide and tetrachloroethene to ethene in a continuous flow column, *J. Contaminant Hydrol.*, 2017.

Bandopadhyay, A., T. Le Borgne, Y. Méheust, and M. Dentz, Enhanced reaction kinetics and reactive mixing scale dynamics in mixing fronts under shear flow for arbitrary damköhler numbers, *Adv. Water Resour.*, *100*, 78–95, 2017.

Beven, K., and P. Germann, Macropores and water flow in soils, *Water resources research*, *18*(5), 1311–1325, 1982.

Briggs, M. A., F. D. Day-Lewis, J. B. Ong, J. W. Harvey, and J. W. Lane, Dual-domain mass-transfer

parameters from electrical hysteresis: Theory and analytical approach applied to laboratory, synthetic streambed, and groundwater experiments, *Water Resour. Res.*, *50*(10), 8281–8299, 2014.

Dahlin, T., and B. Zhou, A numerical comparison of 2d resistivity imaging with 10 electrode arrays, *Geophysical prospecting*, *52*(5), 379–398, 2004.

Day-Lewis, F. D., N. Linde, R. Haggerty, K. Singha, and M. A. Briggs, Pore-network modeling of the electrical signature of solute transport in dual-domain media, *Geophys. Res. Lett.*, *44*, 4908–4916, 2017GL073326, 2017.

Gates, D. D., and R. L. Siegrist, In-situ chemical oxidation of trichloroethylene using hydrogen peroxide, *J. Environ. Eng.*, *121*(9), 639–644, 1995.

Ghosh, U., S. Mandal, and S. Chakraborty, Electroosmosis over charge-modulated surfaces with finite electrical double layer thicknesses: Asymptotic and numerical investigations, *Phys. Rev. Fluids*, *2*, 064,203, 2017.

Haynes, W. M., *CRC handbook of chemistry and physics*, CRC press, 2014.

Hort, R. D., A. Revil, and J. Munakata-Marr, Analysis of sources of bulk conductivity change in saturated silica sand after unbuffered tce oxidation by permanganate, *J. Contam. Hydrol.*, *165*, 11–23, 2014.

Jougnot, D., J. Jimenez-Martinez, R. Legendre, T. Le Borgne, Y. Méheust, and N. Linde, Impact of small-scale saline tracer heterogeneity on electrical resistivity monitoring under saturated and partially saturated conditions: insights from geoelectrical milli-fluidic experiments, *Adv. Water Resour.*, accepted, 2018.

Le Borgne, T., T. R. Ginn, and M. Dentz, Impact of fluid deformation on mixing-induced chemical reactions in heterogeneous flows, *Geophys. Res. Lett.*, *41*(22), 7898–7906, 2014.

Le Borgne, T., M. Dentz, and E. Villermaux, The lamellar description of mixing in porous media, *J. Fluid Mech.*, *770*, 458–498, 2015.

Leal, L. G., *Advanced transport phenomena: fluid mechanics and convective transport processes*, Cambridge University Press, 2007.

Leroy, P., S. Li, D. Jougnot, A. Revil, and Y. Wu, Modelling the evolution of complex conductivity during calcite precipitation on glass beads, *Geophys. J. Inter.*, *209*(1), 123–140, 2017.

Maineult, A., A. Revil, C. Camerlynck, N. Florsch, and K. Titov, Upscaling of spectral induced polarization response using random tube networks, *Geophys. J. Int.*, *209*(2), 948–960, 2017.

Martin, L. R., and D. E. Damschen, Aqueous oxidation of sulfur dioxide by hydrogen peroxide at low ph, *Atmos. Environ.*, *15*(9), 1615–1621, 1981.

Meunier, P., and E. Villermaux, The diffusive strip method for scalar mixing in two dimensions, *J. Fluid Mech.*, *662*, 134–172, 2010.

Nakanishi, K., Prediction of diffusion coefficient of nonelectrolytes in dilute solution based on generalized hammond-stokes plot, *Industrial & Engineering Chemistry Fundamentals*, *17*(4), 253–256, 1978.

Patil, D., and A. Sharma, Study on the corrosion kinetics of iron in acid and base medium, *Journal of Chemistry*, *8*(S1), S358–S362, 2011.

Revil, A., Ionic diffusivity, electrical conductivity, membrane and thermoelectric potentials in colloids and granular porous media: A unified model, *J. Colloid Interf. Sci.*, *212*(2), 503–522, 1999.

Revil, A., and P. Glover, Theory of ionic-surface electrical conduction in porous media, *Phys. Rev. B*, *55*(3), 1757, 1997.

Revil, A., and P. Leroy, Constitutive equations for ionic transport in porous shales, *J. Geophys. Res. B: Solid Earth*, *109*(B3), 2004.

Rossi, F., R. Cucciniello, A. Intiso, A. Proto, O. Motta, and N. Marchettini, Determination of the trichloroethylene diffusion coefficient in water, *AIChE Journal*, *61*(10), 3511–3515, 2015.

Squires, T. M., and M. Z. Bazant, Induced-charge electro-osmosis, *Journal of Fluid Mechanics*, *509*, 217–252, 2004.

Sundstrom, D., H. Klei, T. Nalette, D. Reidy, and B. Weir, Destruction of halogenated aliphatics by ultraviolet catalyzed oxidation with hydrogen peroxide, *Hazard. Waste Hazard Mater.*, *3*(1), 101–110, 1986.

Venkatadri, R., and R. W. Peters, Chemical oxidation technologies: ultraviolet light/hydrogen peroxide, fenton's reagent, and titanium dioxide-assisted photocatalysis, *Hazard. Waste Hazard. Mater.*, *10*(2), 107–149, 1993.

Wang, M., and A. Revil, Electrochemical charge of silica surfaces at high ionic strength in narrow channels, *J. Colloid Interf. Sci.*, *343*(1), 381–386, 2010.

Waxman, M. H., L. Smits, et al., Electrical conductivities in oil-bearing shaly sands, *Society of Petroleum Engineers Journal*, *8*(02), 107–122, 1968.

Zhang, W., Nanoscale iron particles for environmental remediation: an overview, *J. Nanopart. Res.*, *5*(3), 323–332, 2003.